Towards a better understanding of the degradation mechanisms of Li-ion full cells using Si/C composites as anode

Mariana Gutierrez, Mathieu Morcrette, Laure Monconduit, Yohan Oudart, Pierre Lemaire, Carine Davoisne, Nicolas Louvain, Raphaël Janot

Towards a better understanding of the degradation mechanisms of Li-ion full cells using Si/C composites as anode

Mariana Gutierrez [a,b,d], Mathieu Morcrette [b,d], Laure Monconduit [c,d], Yohan Oudart [a], Pierre Lemaire [a], Carine Davoisne [b,d], Nicolas Louvain [c,d], Raphaël Janot [b,d,*]

a) Nanomakers, 1 Rue de Clairefontaine, 78120 Rambouillet, France

b) Laboratoire de Réactivité et Chimie des Solides (LRCS), UMR CNRS 7314, Université de Picardie Jules Verne, Hub de l'énergie, 15 Rue Baudelocque, 80000 Amiens

c) ICGM, Univ. Montpellier, CNRS, ENSCM, Montpellier, France

d) Réseau sur le Stockage Electrochimique de l'Energie (RS2E), FR CNRS 3459, Hub de l'Energie, Amiens, France

* Corresponding author: Raphaël JANOT. Email : raphael.janot@u-picardie.fr

Abstract

Carbon-coated silicon nanoparticles (40 nm diameter) were used to prepare pitch-based Si/C composites with different Si contents and a pitch and graphite-based Si/C/Gr composite. These composites were prepared by pyrolysis at 900°C of a pitch/Si mixture obtained from the dispersion of Si particles in a solution of pitch in THF. The as-prepared composites delivered high coulombic efficiencies at the first cycle (83-86%) and stable reversible capacities (560-650 mAh g^{-1}) versus lithium. The anodes degradation phenomena while cycling versus NMC622 in a full cell configuration were studied by simple electrochemical tests such as analysing the harvested electrodes in half-cells vs. lithium. The clear improvement on electrochemical performances due to the graphite addition was demonstrated with the suppression of the active particle's disconnection. The pitch and graphite-based composite was proven to accommodate well the silicon volume expansion and to deliver a stable electrochemical capacity of 650 mAh g^{-1} at the rate of C/5.

Keywords: Li-ion battery; Si/C composite; full cell; degradation

1. Introduction

Although Li-ion technology is widely used in the energy storage field, the applications are limited by a lack of new and more advanced materials. The usual commercial anode for Li-ion batteries is graphite since it allows the reversible formation of LiC_6 with a specific capacity of 372 mAh g^{-1}. Other materials appear good candidates to increase the battery capacity and to answer the higher energy density demand for other applications such as the electric vehicles [1-4]. Among the candidates, silicon has a strong potential due to its high theoretical capacity (3579 mAh g^{-1}) corresponding to the formation of $Li_{15}Si_4$ [5]. However, its commercialisation has faced severe drawbacks limiting electrodes to low Si contents (< 5 wt.%) and, in addition, silicon is often present as an oxide (SiO_x with x ≤ 2) in order to reduce the electrode mechanical stresses, but this is detrimental to the electrochemical reversibility at the first cycle [6-7]. The main drawback for the use of silicon is that its lithiation leading to $Li_{15}Si_4$ alloy provokes a volume expansion of 270 % ($\Delta V/V_0$) [5,8]. The volume change during electrochemical cycling has multiple consequences such as particles fractures and cracks provoking the eventual disconnection of active material from the electrode and/or current collector [9-10]. In addition to this problem, conventional electrolytes (usually $LiPF_6$ in alkyl carbonates) have a detrimental impact on the Si electrodes. The electrolyte decomposition in contact with the Si surface forms an unstable and non-homogenous SEI (Solid Electrolyte Interphase) [11-15]. During cycling, the fractures on the electrode surface create fresh bare silicon surfaces where electrolyte continuously degrades and form a thick and unstable SEI consuming Li-ions irreversibly. In a half-cell configuration where the lithium inventory is "unlimited", this phenomenon does not provoke a capacity loss. On the other hand, in a full cell configuration, both problems (continuous loss of lithium inventory and anode active material) lead to a fast capacity fading [6, 16-17].

Different solutions have been reported in the literature to try to overcome the issues related to the use of silicon as negative electrode. One of the main modifications is the particles size reduction of silicon [9,13,18-19]. It has been proved that underneath 150 nm in diameter [9-19], the particles fracture is considerably reduced as they can accommodate the mechanical stresses due to the huge volume expansion.

Other studies have been focused on synthesizing Si/C composites from disordered carbon and silicon nanoparticles [13,20-26]. The carbon acts as a buffer layer that helps to accommodate volume expansion and

avoids the direct contact of silicon with the electrolyte. Many carbon precursors have been tested so far but one of the most interesting for later industrialization is petroleum pitch since it is cheap and has a high carbon yield (around 55 % after heat treatment at 900 °C) [27]. After pyrolysis at 900°C, pitch becomes a soft carbon that is a disordered carbon with turbostratic domains of a few nanometers of lateral and stacking dimensions. These carbonaceous structures have generally a BET specific surface area exceeding 10 m^2 g^{-1} and are responsible for significant SEI formation and, thus, lead to high irreversible capacities especially in the first cycles. In half-cell configuration (vs. lithium), these Si/C composites have shown initial coulombic efficiencies (CE) up to 79 % [24-26] and a stable reversible capacity up to 700 mAh g^{-1} for composites containing 17 wt.% of Si [26]. However, in order to increase the first CE and to help to disperse the Si nanoparticles, different works have been devoted to the effect of graphite addition and to the synthesis of Si/C/graphite composites [28-33]. These composites have an enhanced reversibility and first CEs up to 90-93% have been reported [28,33-34]. However, far from an industrial application, most of the electrochemical studies on Si/C or Si/C/Gr composites are done in half-cell configuration where the loss of lithium inventory due to the electrolyte degradation is not detrimental, since the lithium is "unlimited". The electrochemical performances in full cell configuration are less studied. The cycling in this realistic configuration provides more information in terms of failure mechanisms as the loss of lithium inventory will provoke a fast capacity fading [6,16-17]. Even in this configuration, most of the studies show performances for electrodes with low Si loadings representing areal capacities of 1 to 2 mAh cm^{-2} [6,16,17,35], for which the problem related to the loss of active mass due to particles disconnection is limited. Moreover, such silicon loading presents a limited interest for an industrial application. Studies on composites presenting higher areal capacities (> 3 mAh cm^{-2}) and cycled in full cell configuration are fewer [34-37]. In these particular conditions, a composite containing only 9 wt.% of Si shows 92% of initial CE vs. Li and a capacity retention of 96 % after 100 cycles in a full cell configuration with $LiCoO_2$ as the positive electrode [36]. In order to increase the Si content in the commercial electrodes, there is a strong need for identifying the degradation mechanisms in electrodes closer to industrial applications.

In order to have a clear understanding of the impact of the carbon matrix and silicon content on the failure mechanisms, three different composites are studied here. Two Si/carbon composites were firstly prepared using petroleum pitch as precursor with two different Si nanoparticles (Ø = 40 nm) contents: 12 wt.%

and 30 wt.%. Then, a third composite containing 12 wt.% of Si, using not only pitch but also graphite as carbon precursors, was synthetized. Electrodes were prepared from these three composites and tested in half-cell and in full cell configurations. High reversible capacities up to 3 mAh cm^{-2} corresponding to loadings of 3-5 mg cm^{-2} were obtained. The degradation mechanisms in both configurations were identified, correlated and quantified by simple galvanostatic measurements.

2. Experimental method

2.1. Synthesis of Si/C composites

The Si/C composites were prepared from carbon-coated silicon nanoparticles of 40 nm diameter supplied by Nanomakers (labelled SiΩC, cf. Figure S1), petroleum pitch with a softening point of 250°C (PP250) supplied by Rütgers and graphite GHDR 10-4 (Gr) supplied by IMERYS. The SiΩC nanoparticles were produced by laser pyrolysis. This method allows to get nanoparticles from gaseous precursors such as silane (SiH$_4$) and acetylene. The thickness of the carbon layer deposited onto the Si nanoparticles is of the order of 2 nm. Another characteristic of this method is the low content of silicon oxides (~5 %) leading to a higher coulombic efficiency at the first electrochemical cycle.

Three different composites were synthetized by a wet processing method. The masses of pitch, silicon and graphite were adapted in order to get three different compositions as described in Table *1*. PP 250 was dissolved in tetrahydrofuran (THF) for 10 min in an ultrasound bath. Then, the silicon nanoparticles were dispersed in the solution for 1 h of magnetic stirring. For the SiΩC/PP/Gr composites, graphite and pitch were added at the same time. The solvent was evaporated by heating the solution in a silicon oil bath at 75°C. Then, the recovered product was dried in a Büchi B-585 glass oven under vacuum at 90°C for 3 h. The final composite was obtained after pyrolysis in a tubular furnace for 4 h at 400°C followed by 3 h at 900°C under N$_2$ flow (heating ramp of 10°C min^{-1}). For the SiΩC/PP/Gr composite, the masses of SiΩC, pitch and graphite were chosen in order to have the same SiΩC/PP mass ratio as for the 30 % SiΩC/PP composite.

2.2. Physicochemical characterizations

The BET (Brunauer-Emmett-Teller) specific surface area was measured with a Micromeritics ASAP 2020 analyzer. N$_2$ was used as the adsorbed gas at -196°C. The samples were degassed at 30°C for 1 h and

then at 250°C for 12 h under vacuum before analysis. Powder XRD (X-ray diffraction) was performed using a Bruker AXS D8 Advance diffractometer (Cu Kα radiation, $\lambda = 1.5418$ Å). The morphological and textural analyses were performed using a scanning electron microscope (SEM) Quanta 200F (Thermo-Fisher, FEI) through secondary and backscattered electrons images. The microstructure of the silicon/carbon interface was observed using a transmission electron microscope (TEM) Tecnai F20-S-TWIN (Thermo-Fisher, FEI) through high resolution transmission electron microscopy (HRTEM) imaging.

2.3.   Electrochemical tests

The negative electrodes were composed by 80 wt.% of SiΩC/C composite, 2.5 wt.% Vapour Grown Carbon Fibers (VGCF, TM-H Showa Denko), 2.5 wt.% carbon black (Super C45 TIMCAL) and 15 wt.% sodium carboxymethyl-cellulose (CMC, Sigma Aldrich, M_w=250000 g mol^{-1}). For the negative electrode preparation, all the powders were first mixed in a Turbulat equipment for one night. Then, distilled water was added in order to have a dry mass of 27 % of the total mass. The mixture was then stirred in an Ultra-Turrax disperser at 950 rpm for 50 min. The slurry was then casted on a copper film (10 μm thick, TLB-SS Oak-Mitsui). The resulting electrodes had a loading of 3 to 5 mg cm^{-2} meaning an experimental reversible areal capacity of around 3 mAh cm^{-2} for later use in full cell battery configuration. The electrodes were dried at 110°C in a Büchi B-585 glass oven overnight.

The cathode used for the full cell tests was a commercial NMC622 (LiNi$_{0.6}$Mn$_{0.2}$Co$_{0.2}$O$_2$, Nanomyte BE-50E Targray) composed by 90 wt.% NMC, 5 wt.% Carbon Black and 5 wt.% PVDF: this electrode has a reversible capacity of 3 mAh cm^{-2}. The electrochemical characterization was done using CR2032-type coin cells. Whatman glass fibers were used as separator. The electrolyte was a 1 M LiPF$_6$ solution in Propylene Carbonate, Ethylene Carbonate, and Dimethyl Carbonate (PC: EC: DMC, 1:1:3 vol.%) with 5 wt.% Fluoro-Ethylene Carbonate (FEC) and 1 wt.% Vinylidene Carbonate (VC) as additives. A volume of 120 μL of electrolyte was introduced into each coin cell.

Galvanostatic cycling was performed with a BioLogic SAS BCS-805 battery test system at room temperature (T = 24.4 ± 0.5 °C). In half-cell configuration, the negative electrodes were cycled versus Li metal between 10 mV and 1.5 V and the positive electrodes between 4.2 V and 2.5 V. Current rate was indicated as C/n meaning the current applied in order to obtain the theoretical capacity in n hour(s). The cycling conditions

consisted in one formation cycle at C/20 followed by cycling at C/5. For the half-cells, in order to reach complete lithiation, a Constant Voltage (CV) step at 10 mV was added during lithiation until the current is lower than C/100. The full cells were cycled between 4.2 V and 2 V with the first cycle performed at C/20 and the subsequent cycles at C/5. A ratio of negative/positive electrodes equal to 1.1 was used in order to avoid a possible Li plating. In order to balance the full cells, the first discharge areal capacity for the negative electrode vs. Li and the first charge areal capacity of the positive electrode vs. Li were considered: 3.5 and 3.3 mAh cm^{-2}, respectively.

For the post-mortem study, electrodes were harvested after 100 cycles in full cell configuration. They were not dried or washed before studying them in half-cell configuration. Fresh electrolyte was used in the new coin cells.

3.   Results and discussion

3.1.   Characterization of the Si/C composites

Figure 1 presents the XRD patterns of the synthesized composites as well as the precursors. Firstly, the XRD pattern of the SiΩC material is in perfect accordance with crystalline silicon (space group Fd-3m, a = 5.4309 Å). After annealing treatment at 900°C, the XRD of the petroleum pitch shows a broad reflection at about 25° corresponding to the (002) reflection for disordered carbons: the (002) reticular distance (i.e. interlayer spacing of the graphene layers stacking) is about 3.5 Å, much larger than that of graphite (3.35 Å). Even though the pyrolysis allows the graphitization after heat treatment at 2000°C, this process remains very limited at 900°C with the formation of a highly disordered and amorphous carbon, i.e. a soft carbon. At 900°C, only the characteristic reflections of crystalline silicon are visible for all the composites. An increase of the pyrolysis temperature above 900°C would enhance the pitch conductivity, but would also create the undesired electrochemically inactive silicon carbide SiC [38-40].
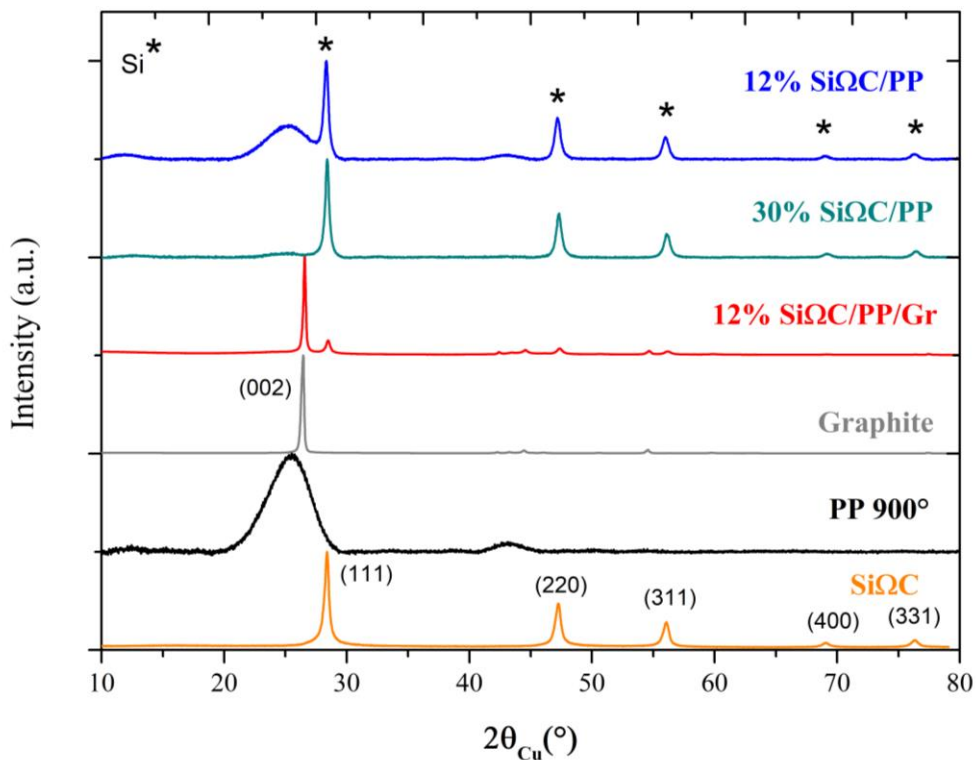
Figure 1: XRD patterns for silicon SiΩC, pyrolyzed pitch, graphite, 12% SiΩC/PP, 30% SiΩC/PP and 12% SiΩC/PP/Gr composites. The stars correspond to the main reflections of crystalline Si.

The composites were also characterized by SEM and TEM to investigate the dispersion of the Si particles inside the different materials. Figure S2 presents the SEM backscattered electron images of each composite. For the three composites, silicon forms agglomerates present all over the carbon surface. As the amount of silicon increases, the covered carbon surface seems to be more important (cf. Figure S2b). In the case of the composites without graphite, large pores (up to 0.5 µm) are visible (cf. Figures S2a and S2b), which could be due to the release of gaseous species occurring upon the pitch pyrolysis. Actually, a significant foaming is observed when pyrolyzing the Si/pitch composite materials. This macro-porosity is useful as it is known that a certain extent of porosity is important to accommodate the silicon volume expansion [24,25]. In addition, the porosity can allow the electrolyte to better impregnate the Si/C composite materials. On the other hand, this kind of porosity was not found on the composite with graphite (cf. Figure S2c) that contains only 28 % of pyrolyzed pitch. We have noticed that the foaming is almost suppressed with the graphite addition. This effect has been already reported in the literature for the pyrolysis of different carbon precursors: the

addition of graphite facilitates the gas release and, thus, the gas release occurs on a much larger temperature range and the foaming is reduced [41].

Figure 2 shows the TEM images of the three composites. In all cases, an amorphous layer of around 2 nm is visible on the Si nanoparticles surface, corresponding to the carbon coating formed by laser pyrolysis, and is highlighted by the white dotted lines drawn in Figures 2b, 2d and 2f. In these high-resolution images, we can see that this amorphous carbon layer constitutes the interface between the crystalline Si particles and the amorphous matrix formed by the pitch pyrolysis. In the three composites, the analysis of the SiΩC particles distribution was done by combining imaging and EDX analyses mapping. Figures 2a and 2c show representative images of the distribution of the SiΩC particles within the carbon matrix of the pitch-based composites. In the bright field images of those samples, the diffraction contrast in the amorphous matrix corresponds to crystalline Si particles (a few Si particles are surrounded by black dash lines). In the Figure 2a, the amorphous matrix (i.e. the soft carbon obtained from the pitch) is interspersed by SiΩC particles while in the Figure 2c, it is fully covered by a high concentration of SiΩC nanoparticles. In Figure 2e, the diffraction contrast observed in the particles (looking like dark ripples across them) highlights the presence of the crystalline graphene sheets of the graphite. On the contrary, the pitch has an amorphous signature allowing us to separate it from the SiΩC particles (few of them surrounded by black dash lines) and the graphite. In this 12% SiΩC/PP/Gr composite, a few areas with a high concentration of SiΩC nanoparticles were also observed. However, in the majority of our observations, the SiΩC particles are more dispersed in the carbon matrix, with even evidence of their presence in between the graphite flakes as observed in Figure 2e.

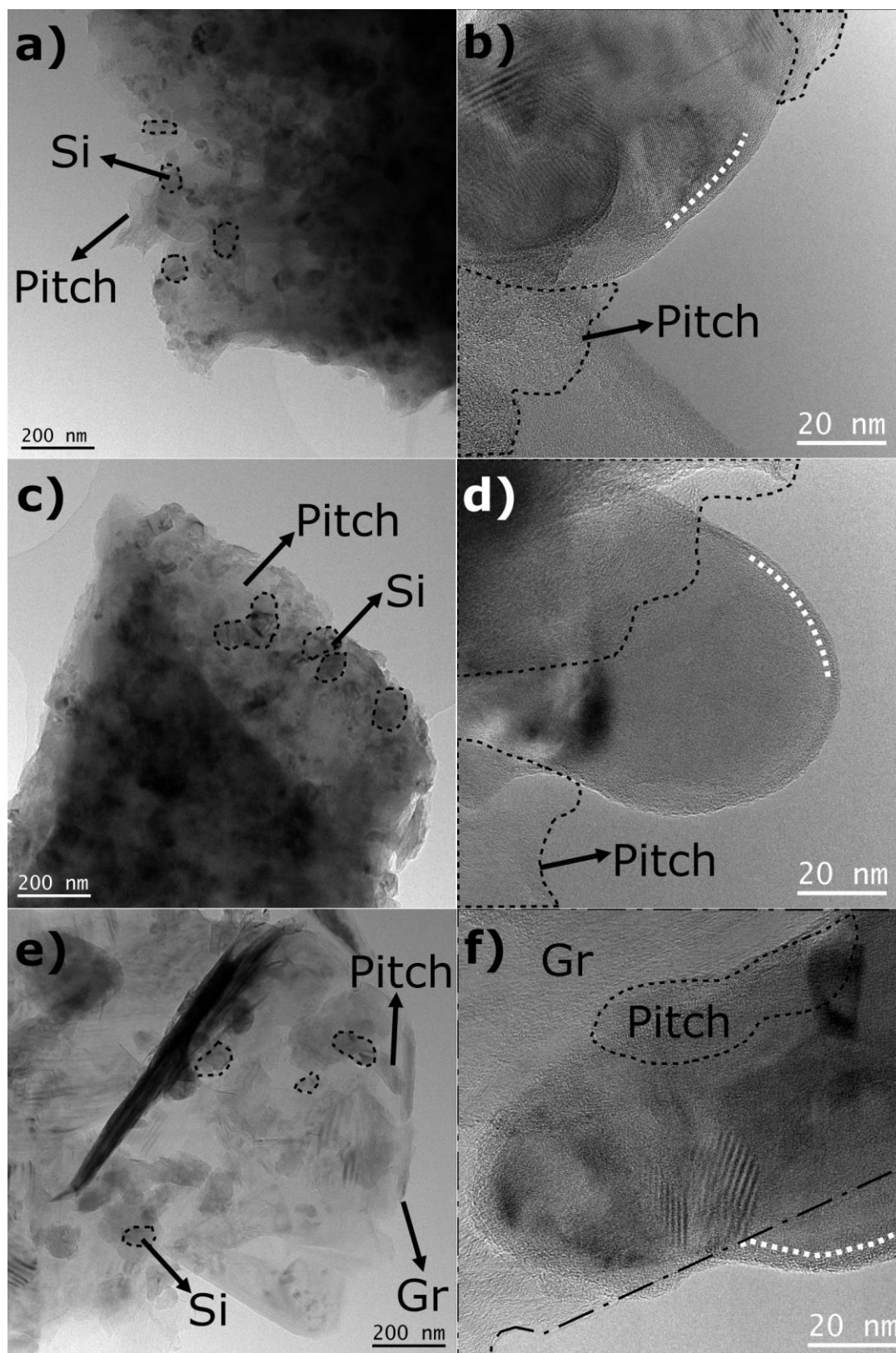Figure 2: TEM images of 12% SiΩC/PP (**a** and **b**), 30% SiΩC/PP (**c** and **d**) and 12% SiΩC/PP/Gr (**e** and **f**). The white dotted lines highlight the amorphous carbon layer (formed by laser pyrolysis) between the Si particles and the pyrolyzed pitch.

3.2. Half-cell electrochemical tests

After synthesis and heat treatment, the composites were grinded and sieved at 80 µm. Before preparing the electrodes, the BET surface areas of the powders were measured. Table 1 presents the values obtained for each composite and the corresponding N_2 adsorption/desorption curves at -196°C can be found in Figure S3 of the supporting information. Even though the silicon nanoparticles have a surface area of around 60 m^2 g^{-1}, the composite containing the highest amount of silicon has the lowest surface area (5 m^2 g^{-1}), emphasizing the good embedding of the Si particles into the carbon matrix. The BET surface area has a direct impact on the SEI formation and, therefore, on the initial coulombic efficiency (ICE) [13]. The 30 % SiΩC/PP composite presents a slightly higher coulombic efficiency than the 12 % SiΩC/PP, reaching 86 % instead of 83 %, which can be explained by its lower BET surface area (5 m^2 g^{-1} vs. 10 m^2 g^{-1}). It is worth noticing that this difference of 3 % in ICE is perfectly reproducible (at least six coins cells were assembled for each composite) and much higher than the error bar of about 0.5 %. On the other hand, the 12 % SiΩC/PP/Gr composite presents a slightly higher surface area (20 m^2 g^{-1}) than the other composites, but the same coulombic efficiency as for the 30 % SiΩC/PP composite, due to the better reversibility of graphite compared to soft carbon (cf. Figure S4).

Table 1: Composition, BET surface area, first coulombic efficiency, theoretical and experimental capacities of the composites.

Composite	Composition (wt.%)	BET surface area (m^2 g^{-1})	1st Coulombic Efficiency (%)	Theoretical capacity (mAh $g^{-1}_{SiΩC/C}$)	Experimental capacity at C/5 (mAh $g^{-1}_{SiΩC/C}$)
12% SiΩC /PP	12/88	8	83	685	560
30% SiΩC /PP	30/70	5	86	1277	1000
12% SiΩC /PP/Gr	12/28/60	20	86	733	650

The electrochemical characterization for both carbon precursors showed that the petroleum pitch pyrolysed at 900°C presents a reversible capacity of 290 mAh g^{-1} compared to 370 mAh g^{-1} for graphite (cf. Figure S4). The lithiation of the pyrolyzed pitch occurs in a large voltage range from 0.8 V to 10 mV contrarily

to graphite for which the Li intercalation occurs below 0.2 V (cf. Figure S4a). The theoretical capacities of the composites, given in Table 1, were calculated based on these reversible capacity experimental values and the capacity of 3579 mAh g^{-1} for silicon (i.e. theoretical capacity corresponding to the Li$_{15}$Si$_4$ formation).

Figure *3* shows the galvanostatic measurements of the SiΩC/C composites in half-cell configuration. From the first cycle at C/20 (cf. Figure *3*a) and the coulombic efficiencies listed in Table 1, all composites present similar first ICEs with 83 % for 12 % SiΩC/PP and 86 % for the two other composites. The first reversible capacities are 580 mAh g^{-1}, 1060 mAh g^{-1} and 660 mAh g^{-1} for the 12% SiΩC/PP, 30% SiΩC/PP and 12% SiΩC/PP/Gr, respectively. At C/20, all three composites show high experimental reversible capacities when compared to the theoretical ones. The pitch-based composites show a capacity representing 84% and 83% of the theoretical capacity for 12% SiΩC/PP and for 30% SiΩC/PP, respectively. On the other hand, the addition of graphite allows to obtain a better lithiation of silicon since the experimental reversible capacity reaches 90% of the theoretical one for the 12 % SiΩC/PP/Gr composite.

The cycling at C/5 (cf. Figure 3b) shows experimental reversible capacities of 560 mAh g^{-1}, 1000 mAh g^{-1} and 650 mAh g^{-1} for 12 % SiΩC/PP, 30 % SiΩC/PP and 12 % SiΩC/PP/Gr, respectively, very close to the capacities recorded previously at C/20. The dQ/dV plot shows that, even at C/5, the full lithiation of Si was achieved for all composites as the peak corresponding to the Li$_{15}$Si$_4$ delithiation is observed at 0.45 V upon oxidation (cf. Figure S5). The composites containing 12 wt.% of silicon with and without graphite present a stable capacity retention. However, a difference between the composites is observed as the composite containing graphite presents the highest coulombic efficiency values at each cycle (cf. Figure 3b). As expected, the increasing amount of silicon has detrimental consequences for the capacity retention. A progressive fade in capacity and coulombic efficiency is observed for the 30 % SiΩC/PP composite.
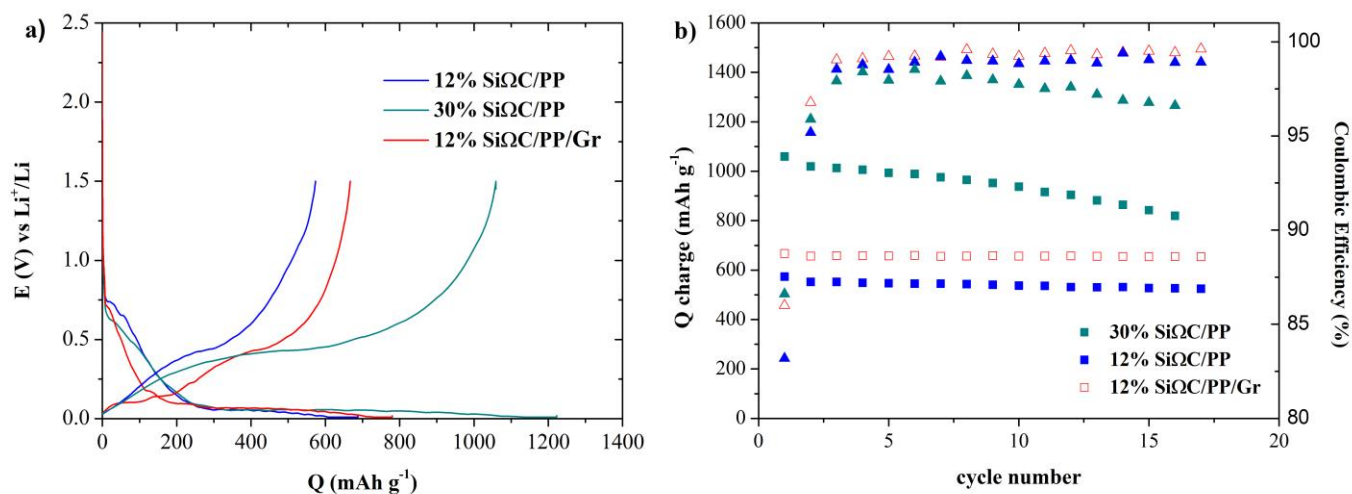
Figure 3: Half-cells of the SiΩC/C composites a) first galvanostatic curves at C/20 of SiΩC/C composites vs. Li and b) charge capacity retention of SiΩC/C composites vs. Li at C/5.

Table 1 resumes the experimental reversible capacities of the different composites at C/5. The silicon capacity contribution was calculated from the experimental reversible capacities of the composites and of the carbon precursors. The pitch-based composites present similar Si capacity contributions corresponding to 72% and 74% of the Si theoretical capacity for 12% SiΩC/PP and 30% SiΩC/PP, respectively. The graphite-based composite presents a higher silicon capacity representing 81% of the theoretical one. This could be explained by an enhancement on the electronic percolation by adding graphite and, thus, a deeper lithiation/delithiation of the Si nanoparticles.

After 20 cycles in half-cell configuration, the galvanostatic data starts showing electrochemical failure with extremely high charge capacity values resulting in coulombic efficiencies higher than 100%. The cells were then stopped, opened and a lithium dendritic growth phenomenon was observed on the lithium disc and through the separator for all three samples. For this reason, the capacity retention in half-cells can only be studied for the first few cycles. However, in order to better understand the benefits of "diluting" the pitch-based composites with graphite, a study of the irreversible capacity was done. As in other studies [20,42-46] and, as illustrated in Figure 4, the hypothesis was made that only two phenomena are responsible for the irreversible capacity and coulombic efficiency degradation in a half-cell configuration. First, during the first discharge (i.e. lithiation), the Li$^+$ ions are partially consumed by the electrolyte degradation through lithium carbonates, LiF and other species formation. During cycling, as bare surfaces of the electrode are created due

to the large volume change, new SEI will continue to be formed. Then, during delithiation, the expanded particles shrink. The electrode fractures during lithiation/delithiation can provoke the disconnection of particles. These isolated particles cannot contribute anymore to the capacity. For these reasons, it is considered that the sole phenomenon responsible for the irreversible capacity during lithiation is the SEI formation and, during delithiation, is the active mass disconnection.
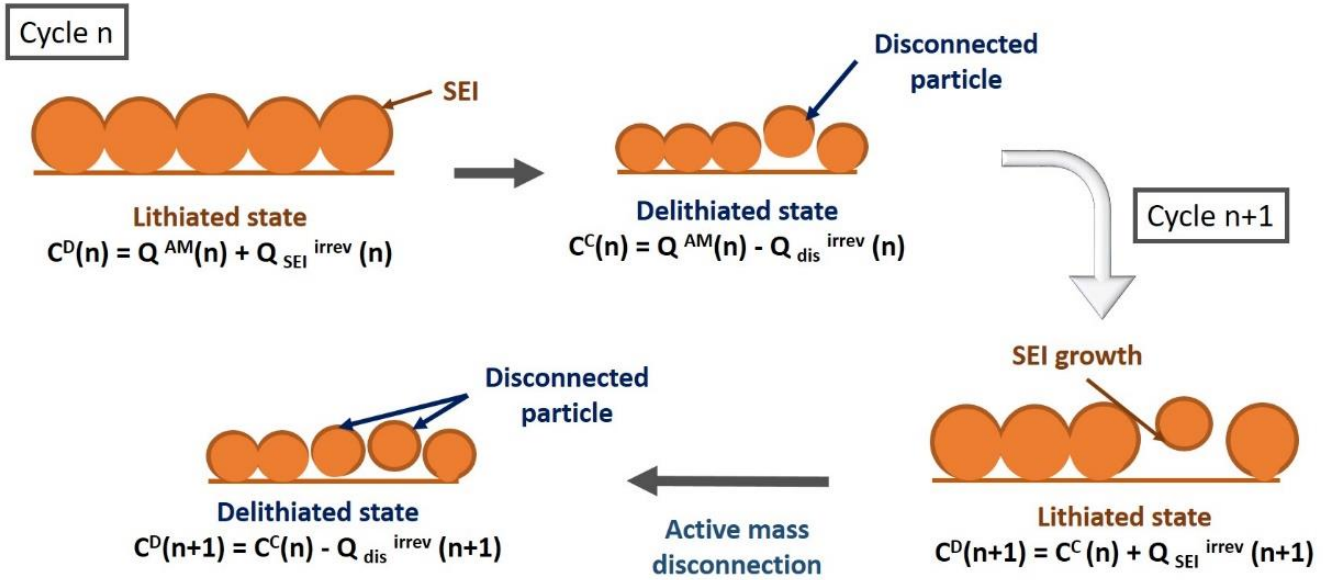

Figure 4: Degradation mechanisms for Si/C composites in half-cell configuration.

From Figure 4 and similarly to other works [20,42-46], the different capacity losses contributions are defined as:

$$Q^{ir}_{total} (n) = C^D (n) - C^C (n)$$

$$Q^{ir}_{disc} (n+1) = C^C (n) – C^C (n+1)$$

$$Q^{ir}_{SEI} (n+1) = C^D (n+1) – C^C (n)$$

with:

➢ $C^D(n)$: discharge capacity at cycle n,

➢ $C^C(n)$: charge capacity at cycle n,

➢ $Q^{AM}(n)$: active mass capacity

➢ $Q^{ir}_{total} (n)$: total irreversible capacity at cycle n,

➢ $Q^{ir}_{disc} (n+1)$: irreversible capacity due to active mass disconnection at cycle n+1,

➢ $Q^{ir}_{SEI} (n+1)$: irreversible capacity due to degradation of the electrolyte at cycle n+1.

From the experimental half-cell cycling data, the cumulative capacity loss for each degradation mechanism was calculated from the second cycle (same current rate of C/5) and plotted as shown in Figure 5a and 5b. Figure 5b shows the fast increase of the capacity loss due to the electrolyte degradation and SEI formation for the three composites and it increases all the more as the composite is silicon rich. For the composites with 12% SiΩC content, with or without graphite, the loss due to SEI increases continuously and at the same rate, whilst for the 30% SiΩC, it increases much more rapidly. The SEI growth seems to be directly related to the silicon amount and the addition of graphite has no clear impact.

Figure 5a shows the capacity loss due to disconnection of active material in the electrode. In this case, an important difference can be observed between the three composites. For the electrodes without graphite, the capacity loss is much more important especially for higher silicon content. As the amount of silicon increases, the mechanical instability of the electrode increases dramatically likely because there is less carbon to accommodate the volume change. Even if, for the 12% SiΩC/PP composite, the irreversible capacity due to active mass disconnection is lower than for 30% SiΩC/PP composite, the disconnection losses still represent 35 % of the total cumulative irreversible capacity after 15 cycles. On the other hand, this study shows that the 12 % SiΩC/PP/Gr presents no capacity loss due to active material disconnection. This would mean that the addition of graphite to the composite results in a matrix with mechanical properties more suitable for accommodating the silicon volume expansion. This could be also related to the difference in microstructure observed by TEM for the three samples. In the case of pitch-based composites, some areas exhibit high concentration of Si particles, where the lithiation could induce locally a very important mechanical stress. In the composite with graphite, the Si nanoparticles have a much better dispersion within the carbon matrix allowing the volume change to be more homogeneous in the electrode. However, besides the silicon nanoparticles distribution, the addition of graphite has likely a strong impact on the mechanical properties. Further studies, such as indentation of the electrodes, are under way to characterize their mechanical properties (elasticity/plasticity).
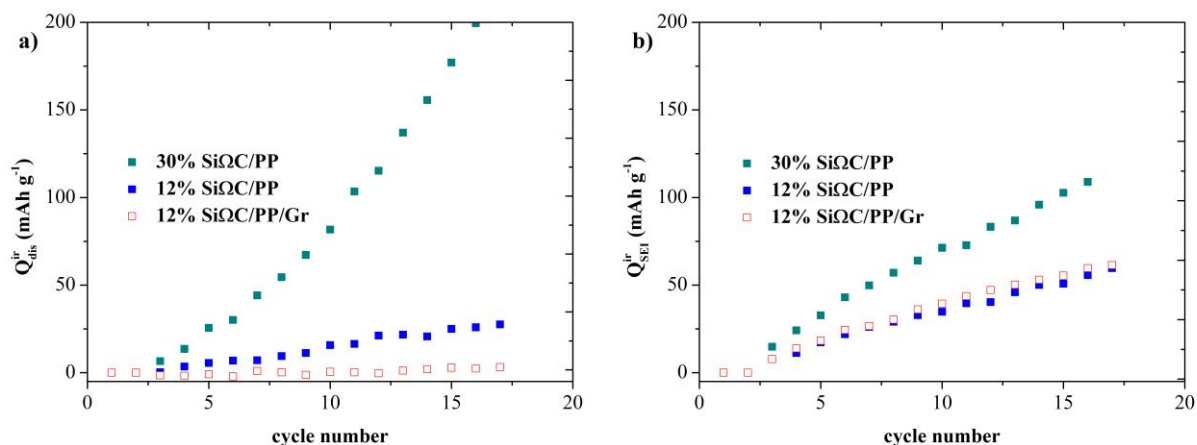
Figure 5: Cumulative irreversible capacity due to: a) active particles disconnection and b) electrolyte degradation.

3.3. Full cell electrochemical tests: Si/C vs NMC

To further investigate the capacity retention for each composite, the electrodes were cycled in a full cell configuration using NMC622 as cathode, the electrochemical performances of the latter vs. Li being presented in Figure S6. The negative to positive electrodes ratio was studied and defined to 1.1 in order to avoid Li plating but nevertheless have a full lithiation of the silicon. Figure 6 shows the full cell electrochemical performances of the different composites. A progressive capacity fading can be seen for all the materials. After 97 cycles, at C/5, the composites present a capacity retention (Q^{97th}/Q^{2nd}) of 38% for *12% SiΩC/PP,* 23% for 30% SiΩ*C/PP* and 58% for *12% SiΩC/PP/Gr*. The composite containing graphite presents therefore the highest capacity retention and coulombic efficiency. The capacity retention in the full cell configuration agrees well with the study of the irreversible capacity in half-cell configuration. The normalized capacities of each composite at the first cycle at C/20 are shown in Figure S7. While all composites show similar ICE (83-85%), the composite containing graphite presents less polarization than the other two composites. Compared to pitch or silicon, graphite is the material presenting the lowest polarization during insertion/disinsertion mechanism. The main difference in polarization can be seen during the early stage of discharge corresponding to delithiation of graphite explaining the lower polarisation for the electrode containing graphite.
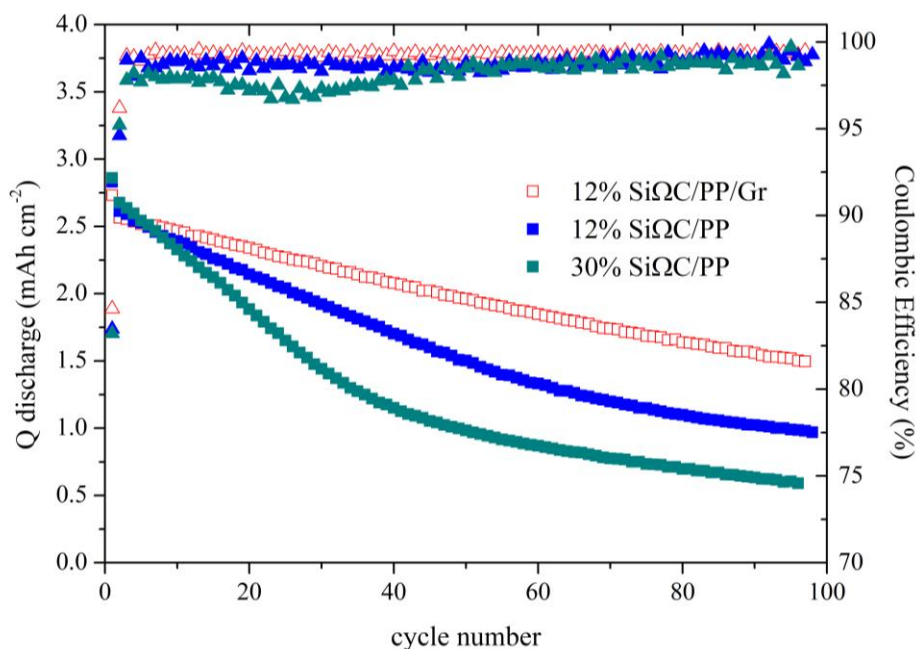
Figure 6: Electrochemical performances of Si/C composites in a full cell configuration using NMC622 as the cathode.

In a full cell configuration, multiple phenomena can contribute to the capacity fading. Contrarily to the cycling in half-cells vs. Li, there is a limited amount of lithium in full cells. One of the reasons for capacity fading is the loss of active material, either from the cathode, or the anode. According to the material studied at the positive electrode and its electrochemical performances in half-cells (cf. Figure S7), we can consider that there is no loss of cathode active material. So, one possibility of capacity fading can be explained by loss of active materials and, especially, silicon. In this case, the composite capacity will decrease, meaning a loss of full cell capacity, but also the full cell can start to be unbalanced provoking the lithium loss in the form of Li plating. A second phenomenon can be the electrolyte decomposition. Even if there is no loss of anode active material, the capacity fading could be explained by a constant growth of the SEI that will consume Li^+ irreversibly. Generally, the capacity fading is a combination of all these mentioned phenomena.

In order to further investigate the causes of capacity fading, both the negative and the positive electrodes were harvested after cycling in full cells and they were then cycled versus Li metal in half-cells.

3.4. Post-mortem cycling in half-cells

Post-mortem electrochemical measurements were done in order to investigate the causes of loss of capacity retention for each material. After 97 cycles and full discharge down to 2.0 V, the full cells were opened, the electrodes were collected and they were then cycled vs. Li in half-cells. Figure 7 shows the electrochemical data of the full cells and their respective post-mortem half-cells for the three composites. The full cells are denominated depending on the anode used as defined in Table 2. The results of the post-mortem cycling of *Full cell 1* and *Full cell 2* using the pitch-based composites as anodes are presented in Figure 7a and 7b, respectively. Figure 7c presents the results for *Full cell 3*. Table 2 resumes the reversible capacities of the full cells at 2nd and 97th cycles as well as the corresponding charge and discharge capacities of the harvested electrodes in half-cell configuration after cycling in full cells.

Table 2: Composition of the full cells, the harvested electrodes and their corresponding capacities.

Full cell denomination	Q 2nd discharge (mAh cm^{-2})	Q 97th discharge (mAh cm^{-2})	Electrodes cycled vs Li after 97 cycles in full cell	Q 1st charge (mAh cm^{-2})	Q 1st discharge (mAh cm^{-2})
Full cell 1	2.6	1.0	NMC 1	0.6	2.6
			12% SiΩC/PP	1.8	2.5
Full cell 2	2.7	0.6	NMC 2	0.2	2.4
			30% SiΩC/PP	1.1	1.7
Full cell 3	2.6	1.5	NMC 3	1.3	2.6
			12% SiΩC/PP/Gr	2.7	3.2

For the NMC622, the first charge capacity of the harvested electrode corresponds to its delithiation after full cell complete lithiation. Therefore, the initial charge capacities of 0.6 mAh cm^{-2} for *NMC 1*, 0.2 mAh cm^{-2} for *NMC 2* and 1.3 mAh cm^{-2} for NMC 3 represent the amount of lithium still available in each cathode for cycling at a cut-off potential of 4.2 V. It is worth noticing that the charge capacities of the NMC do not correspond exactly to the capacity at the 97th cycle in full cell configuration. In a full cell configuration, the

potential of each electrode cannot be controlled. Initially, the NMC delithiation potential is 4.2 V. However, as the system starts losing capacity during cycling, the delithiation cut-off potential of the positive electrode is higher in order to compensate the loss of lithium during the previous lithiation. For this reason, when cycling again at a cut-off potential of 4.2 V, the NMC capacities are lower than the capacities of the full cell at the last cycle. Then, during lithiation in half-cell, Figure 7 shows that NMC *1* and *NMC 3* recover the full reversible capacities obtained in full cell configuration (2.6 mAh cm^{-2}) and continue to cycle with a stable capacity. It can be concluded that there is a loss of lithium inventory, either from SEI growth, or loss of anode active mass or both phenomena. On the other hand, in the case of *NMC 2,* the NMC recovers only 90 % of the reversible capacity during the first lithiation. However, it recovers the full reversible capacity during the second cycle. *NMC 2* is the electrode that presents the highest difference between 1st charge capacity in half-cell and the 97th capacity in full cell, meaning that this electrode was cycled at higher potential than the other two.

In the case of the anodes, a difference between pitch-based composites and pitch and graphite-based composite is clearly observed. In the case of the pitch-based composites, the harvested anodes presented a reversible capacity of 1.8 mAh cm^{-2} for the 12 % SiΩC/PP and 1.1 mAh cm^{-2} for the 30 % SiΩC/PP anodes (cf. Figures 7a and 7b, respectively). Only 70 % of the initial reversible capacity is recovered for the 12 % SiΩC/PP and 40 % for the 30 % SiΩC/PP meaning both anodes show loss of active material during cycling. However, the recovered capacities are higher than the 97th capacities on full cell configuration. This means that a part of capacity fading was also due to lithium consumption for electrolyte decomposition. It can be concluded for the pitch-based composites that the full cell capacity fading is explained by both phenomena: loss of anode active mass and SEI growth. Also, the higher content of silicon has detrimental consequences for capacity retention. This agrees well with the study of the irreversible capacities in half-cell configuration.
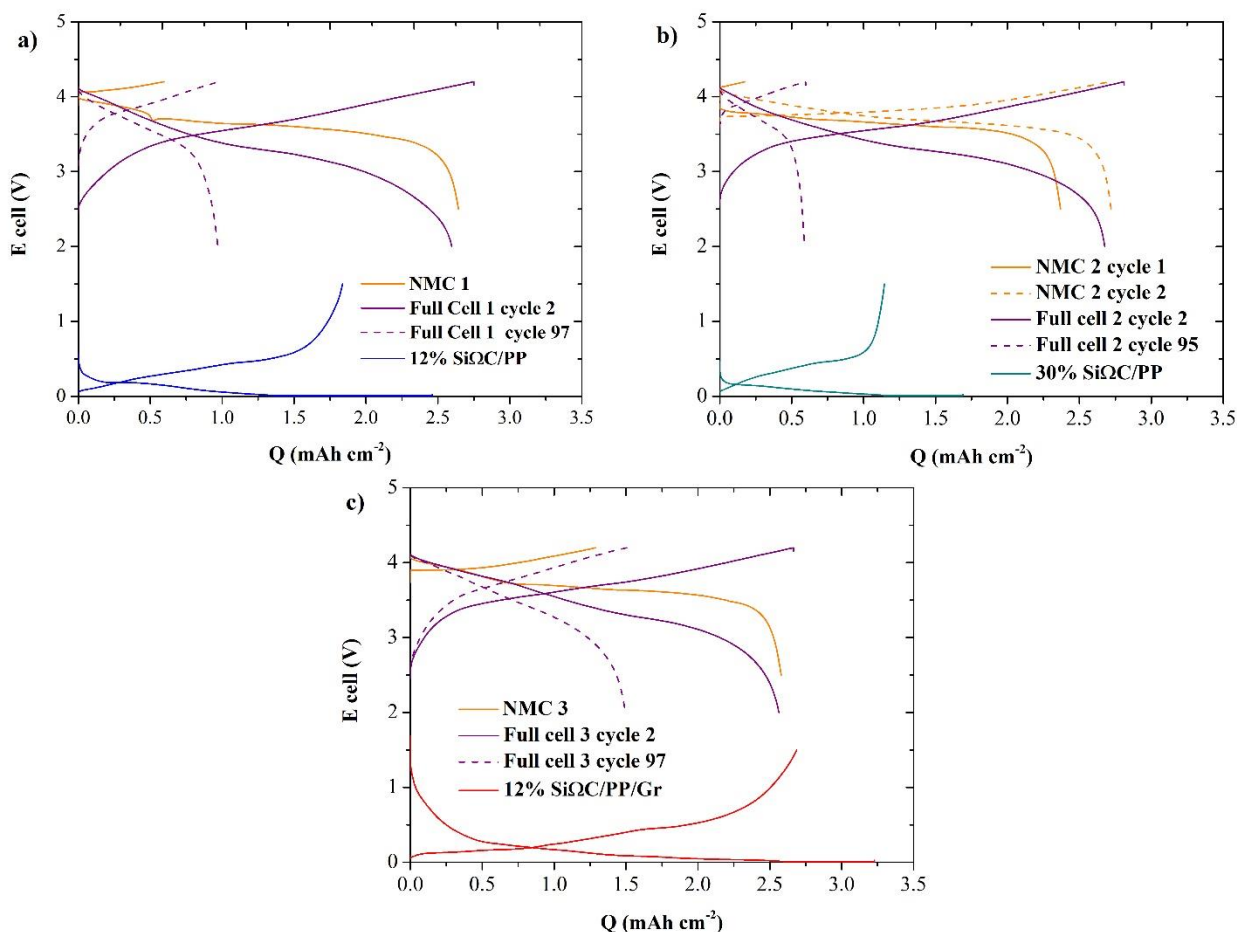
Figure 7: Galvanostatic curves of the full cell and its corresponding harvested electrodes in half-cells:

a)12% SiΩC/PP, b) 30% SiΩC/PP and c) 12% SiΩC/PP/Gr.

In the case of the 12% SiΩC/PP/Gr anode (cf. Figure 7c), after the first discharge, the anode recovers the reversible capacity obtained in full cell configuration (2.7 mAh cm^{-2}). There is no loss of active mass since the complete reversible capacity is recovered. The SiΩC/PP/Gr composite presents a capacity loss due solely to the SEI degradation. The study in half-cell is thus confirmed and validated. The double carbon matrix (by pitch and graphite addition) is demonstrated to accommodate the Si volume change efficiently for 97 cycles in a full cell configuration. As mentioned in the case of the study in half-cell configuration, the addition of graphite seems to contribute to the enhancement of the mechanical properties of the carbon matrix allowing it to better accommodate the volume change during cycling. However, characterizations of the mechanical properties of the composite and/or the electrode are still needed to fully demonstrate such a benefit effect of graphite addition.

4. Conclusions

A simple synthesis method allowed the preparation of three different Si/C composites with low BET surfaces areas: 12% SiΩC/PP, 30% SiΩC/PP and 12% SiΩC/PP/Gr. These composites showed high coulombic efficiencies at the first cycles ranging from 83 to 86%. The composites containing 12% of silicon showed good electrochemical stability in half-cell configuration and reversible capacities of 650 mAh g^{-1} and 560 mAh g^{-1} for 12 % SiΩC/PP/Gr and 12 % SiΩC/PP, respectively. It was demonstrated that the addition of graphite enhances the electrode reversibility. The analytical study of the irreversible capacity contributions showed no loss due to active mass disconnection for 12% SiΩC/PP/Gr contrarily to the pitch-based composites.

The study in full cell configuration vs. NMC622 and the post-mortem cycling of the harvested electrodes confirmed the first analysis in half-cells regarding the irreversible capacity losses of the composites. Indeed, while the pitch-based composites showed capacity fading due to both loss of anode active mass and electrolyte degradation, the composite containing graphite showed no active mass disconnection. It can be concluded that the addition of graphite in the Si/C composites improves its ability to accommodate the silicon volume expansion.

Further studies are still necessary in order to characterize the mechanical properties of the composite and/or the electrode, to better understand the electrolyte decomposition and new electrolytes will be tested with the hope of improving the capacity retention.

References

[1]   J.M. Tarascon, M. Armand, Issues and challenges facing rechargeable lithium batteries, Nature. 414 (2001) 359–367. https://doi.org/10.1038/35104644

[2]   V. Pellegrini, S. Bodoardo, D. Brandell, K. Edström, Challenges and perspectives for new material solutions in batteries, Solid State Commun. 303–304 (2019) 113733. https://doi.org/10.1016/j.ssc.2019.113733.

[3]   Z. Lin, T. Liu, X. Ai, C. Liang, Aligning academia and industry for unified battery performance metrics, Nat. Commun. 9 (2018) 5262. https://doi.org/10.1038/s41467-018-07599-8.

[4]   S. He, S. Huang, S. Wang, I. Mizota, X. Liu, X. Hou, Considering critical factors of silicon/graphite anode materials for practical high-energy lithium-ion battery applications, Energy Fuels. 35 (2021) 944–964. https://doi.org/10.1021/acs.energyfuels.0c02948.

[5]   M.N. Obrovac, L. Christensen, Structural changes in silicon anodes during lithium insertion/ extraction, Electrochem. Solid-State Lett. (2004) 7 (5) A93. https://doi.org/10.1149/1.1652421

[6]   X. Li, A.M. Colclasure, D.P. Finegan, D. Ren, Y. Shi, X. Feng, L. Cao, Y. Yang, K. Smith, Degradation mechanisms of high capacity 18650 cells containing Si-graphite anode and nickel-rich NMC cathode, Electrochimica Acta. 297 (2019) 1109–1120. https://doi.org/10.1016/j.electacta.2018.11.194.

[7]   T.M.M. Heenan, A. Jnawali, M.D.R. Kok, T.G. Tranter, C. Tan, A. Dimitrijevic, R. Jervis, D.J.L. Brett, P.R. Shearing, An advanced microstructural and electrochemical datasheet on 18650 Li-ion batteries with nickel-rich NMC811 cathodes and graphite-silicon anodes, J. Electrochem. Soc. 167 (2020) 140530. https://doi.org/10.1149/1945-7111/abc4c1.

[8]   M.N. Obrovac, L.J. Krause, Reversible Cycling of Crystalline Silicon Powder, J. Electrochem. Soc. 154 (2007) A103. https://doi.org/10.1149/1.2402112.

[9]   M.T. McDowell, S.W. Lee, W.D. Nix, Y. Cui, 25th anniversary article: Understanding the lithiation of silicon and other alloying anodes for lithium-ion batteries, Adv. Mater. 25 (2013) 4966–4985. https://doi.org/10.1002/adma.201301795.

[10]   M.J. Chon, V.A. Sethuraman, A. McCormick, V. Srinivasan, P.R. Guduru, Real-time measurement of stress and damage evolution during initial lithiation of crystalline silicon, Phys. Rev. Letters 12 (2011). https://doi.org/10.1103/PhysRevLett.107.045503

[11]   B. Philippe, R. Dedryvère, J. Allouche, F. Lindgren, M. Gorgoi, H. Rensmo, D. Gonbeau, K. Edström, Nanosilicon electrodes for lithium-ion batteries: Interfacial mechanisms studied by hard and soft X-ray photoelectron spectroscopy, Chem. Mater. 24 (2012) 1107–1115. https://doi.org/10.1021/cm2034195.

[12]   P. Verma, P. Maire, P. Novák, A review of the features and analyses of the solid electrolyte interphase in Li-ion batteries, Electrochimica Acta. 55 (2010) 6332–6341. https://doi.org/10.1016/j.electacta.2010.05.072.

[13]   M.N. Obrovac, V.L. Chevrier, Alloy negative electrodes for Li-ion batteries, Chem. Rev. 114 (2014) 11444–11502. https://doi.org/10.1021/cr500207g.

[14]   C. Pereira-Nabais, J. Światowska, A. Chagnes, F. Ozanam, A. Gohier, P. Tran-Van, C.-S. Cojocaru, M. Cassir, P. Marcus, Interphase chemistry of Si electrodes used as anodes in Li-ion batteries, Applied Surface Science. 266 (2013) 5–16. https://doi.org/10.1016/j.apsusc.2012.10.165.

[15]   D. Aurbach, A comparative study of synthetic graphite and Li electrodes in electrolyte solutions based on ethylene carbonate-dimethyl carbonate mixtures, J. Electrochem. Soc. 143 (1996) 3809. https://doi.org/10.1149/1.1837300.

[16]   N. Delpuech, N. Dupre, P. Moreau, J.-S. Bridel, J. Gaubicher, B. Lestriez, D. Guyomard, Mechanism of silicon electrode aging upon cycling in full lithium-ion batteries, Chem. Sus. Chem. 9 (2016) 841–848. https://doi.org/10.1002/cssc.201501628.

[17]   S.E. Trask, K.Z. Pupek, J.A. Gilbert, M. Klett, B.J. Polzin, A.N. Jansen, D.P. Abraham, Performance of full cells containing carbonate-based LiFSI electrolytes and silicon-graphite negative electrodes, J. Electrochem. Soc. 163 (2016) A345–A350. https://doi.org/10.1149/2.0981602jes.

[18]   J. Graetz, C.C. Ahn, R. Yazami, B. Fultz, Highly reversible lithium storage in nanostructured silicon, Electrochem. Solid State Lett. 6 (2003) A194. https://doi.org/10.1149/1.1596917.

[19]   X.H. Liu, L. Zhong, S. Huang, S.X. Mao, T. Zhu, J.Y. Huang, Size-dependent fracture of silicon nanoparticles during lithiation, ACS Nano. 6 (2012) 1522–1531. https://doi.org/10.1021/nn204476h.

[20]   J. Saint, Matériaux d'électrode négative pour accumulateurs à ions lithium : Etude des systèmes binaires Li-Ga et Li-B et des composites silicium-carbone, Université de Picardie Jules Verne, PhD thesis (2005).

[21]   A.M. Escamilla-Pérez, A. Roland, S. Giraud, C. Guiraud, H. Virieux, K. Demoulin, Y. Oudart, N. Louvain, L. Monconduit, Pitch-based carbon/nano-silicon composite, an efficient anode for Li-ion batteries, RSC Adv. 9 (2019) 10546–10553. https://doi.org/10.1039/C9RA00437H.

[22]   Y. Yong, L.-Z. Fan, Silicon/carbon nanocomposites used as anode materials for lithium-ion batteries, Ionics. 19 (2013) 1545–1549. https://doi.org/10.1007/s11581-013-0886-1.

[23]   W. Xing, Pyrolysed pitch-polysilane blends for use as anode materials in lithium ion batteries, Solid State Ionics. 93 (1997) 239–244. https://doi.org/10.1016/S0167-2738(96)00512-7.

[24]   H. Dong, In-situ construction of porous Si@C composites with LiCl template to provide silicon anode expansion buffer, Carbon 173 (2021) 687-695.https://doi.org/10.1016/j.carbon.2020.11.042

[25]   Y. He, F. Han, F. Wang, J. Tao, H. Wu, F. Zhang, J. Liu, Optimal microstructural design of pitch-derived soft carbon shell in yolk-shell silicon/carbon composite for superior lithium storage, Electrochimica Acta. 373 (2021) 137924. https://doi.org/10.1016/j.electacta.2021.137924.

[26]   C.-Y. Chen, A.-H. Liang, C.-L. Huang, T.-H. Hsu, Y.-Y. Li, The pitch-based silicon-carbon composites fabricated by electro-spraying technique as the anode material of lithium ion battery, J. All. Comp. 844 (2020) 156025. https://doi.org/10.1016/j.jallcom.2020.156025.

[27]   Y. Li, Y.-S. Hu, H. Li, L. Chen, X. Huang, A superior low-cost amorphous carbon anode made from pitch and lignin for sodium-ion batteries, J. Mater. Chem. A. 4 (2016) 96–104. https://doi.org/10.1039/C5TA08601A.

[28]   C. Xiao, P. He, J. Ren, M. Yue, Y. Huang, X. He, Walnut-structure Si–G/C materials with high coulombic efficiency for long-life lithium ion batteries, RSC Adv. 8 (2018) 27580–27586. https://doi.org/10.1039/C8RA04804E.

[29]   Y.S. Yoon, S.H. Jee, S.H. Lee, S.C. Nam, Nano Si-coated graphite composite anode synthesized by semi-mass production ball milling for lithium secondary batteries, Surface and Coatings Technology. 206 (2011) 553–558. https://doi.org/10.1016/j.surfcoat.2011.07.076.

[30]   M. Li, X. Hou, Y. Sha, J. Wang, S. Hu, X. Liu, Z. Shao, Facile spray-drying/pyrolysis synthesis of core–shell structure graphite/silicon-porous carbon composite as a superior anode for Li-ion batteries, J. Power Sources. 248 (2014) 721–728. https://doi.org/10.1016/j.jpowsour.2013.10.012.

[31]   Lee, Eun Hee, Jeong, Bo Ock, Jeong, Seong Hun, Kim, Tae Jeong, Kim, Yong Shin, Jung, Yongju, Effect of carbon matrix on electrochemical performance of Si/C composites for use in anodes of lithium secondary batteries, Bulletin of the Korean Chemical Society. 34 (2013) 1435–1440. https://doi.org/10.5012/BKCS.2013.34.5.1435.

[32]   S. Chae, S. Choi, N. Kim, J. Sung, J. Cho, Integration of graphite and silicon anodes for the commercialization of high-energy lithium-ion batteries, Angew. Chem. Int. Ed. 59 (2020) 110–135. https://doi.org/10.1002/anie.201902085.

[33]   M. Ko, S. Chae, J. Ma, N. Kim, H.-W. Lee, Y. Cui, J. Cho, Scalable synthesis of silicon-nanolayer-embedded graphite for high-energy lithium-ion batteries, Nat. Energy. 1 (2016) 16113. https://doi.org/10.1038/nenergy.2016.113.

[34]   N. Kim, Fast-charging high-energy lithium-ion batteries via implantation of amorphous silicon nanolayer in edge-plane activated graphite anodes, Nature Commun. 8 (2017) 812. https://doi.org/10.1038/s41467-017-00973-y

[35]   S. Chae, S.-H. Choi, N. Kim, J. Sung, J. Cho, Integration of graphite and silicon anodes for the commercialization of high-energy lithium-ion Batteries, Angew. Chem. Int. Ed. (2020) 26. https://doi.org/10.1002/anie.201902085

[36]   M. Ko, S. Chae, J. Ma, N. Kim, H.-W. Lee, Y. Cui, J. Cho, Scalable synthesis of silicon-nanolayer-embedded graphite for high-energy lithium-ion batteries, Nat. Energy. 1 (2016) 16113. https://doi.org/10.1038/nenergy.2016.113.

[37]   F. Aupperle, G.G. Eshetu, K.W. Eberman, A. Xioa, J.-S. Bridel, E. Figgemeier, Realizing a high-performance $LiNi_{0.6}Mn_{0.2}Co_{0.2}O_2$ /silicon–graphite full lithium ion battery cell *via* a designer electrolyte additive, J. Mater. Chem. A. 8 (2020) 19573–19587. https://doi.org/10.1039/D0TA05827K.

[38]   M. C. Ovin Ania, Pitch-Based Carbon Materials, ITA (2007).

[39]   C. Paireau, S. Jouanneau, M.-R. Ammar, P. Simon, F. Béguin, E. Raymundo-Piñero, Si/C composites prepared by spray drying from cross-linked polyvinyl alcohol as Li-ion batteries anodes, Electrochimica Acta. 174 (2015) 361–368. https://doi.org/10.1016/j.electacta.2015.06.016.

[40]   Y. Li, W. Liu, Z. Long, P. Xu, Y. Sun, X. Zhang, S. Ma, N. Jiang, Si@C microsphere composite with multiple buffer structures for high-performance lithium-ion battery anodes, Chemistry - A European Journal. 24 (2018) 12912–12919. https://doi.org/10.1002/chem.201801417.

[41]   N. Daher, Synthèses de carbones durs comme électrode négative de batteries Na-ion, Université de Picardie Jules Verne, PhD Thesis (2020).

[42]   A. Touidjine, Optimisation de l'électrode négative à base de silicium pour les batteries lithium-ion, Université de Picardie Jules Verne, PhD thesis (2016).

[43]   M. Gauthier, D. Mazouzi, D. Reyter, B. Lestriez, P. Moreau, D. Guyomard, L. Roué, A low-cost and high-performance ball-milled Si-based negative electrode for high-energy Li-ion batteries, Energy Environ. Sci. 6 (2013) 2145. https://doi.org/10.1039/c3ee41318g.

[44]   S.Y. Sayed, W.P. Kalisvaart, B.C. Olsen, E.J. Luber, H. Xie, J.M. Buriak, Alternating silicon and carbon multilayer-structured anodes suppress formation of the c-Li$_{3.75}$Si phase, Chem. Mater. 31 (2019) 6578–6589. https://doi.org/10.1021/acs.chemmater.9b00389.

[45]   H. Xie, S.Y. Sayed, W.P. Kalisvaart, S.J. Schaper, P. Mu, E.J. Luber, B.C. Olsen, M. Haese, J.M. Buriak, Adhesion and surface layers on silicon anodes suppress formation of c-Li$_{3.75}$Si and Solid-Electrolyte Interphase, ACS Appl. Energy Mater. 3,2 (2020) 1609-1616. https://doi.org/10.1021/acsaem.9b02090

[46]   A. Roland, B. Delarre, J.-B. Ledeuil, N. Louvain, H. Martinez, L. Monconduit, Silicon-based electrodes formulation in buffered solution for enhanced electrode-electrolyte interfaces, J. Power Sources. 489 (2021) 229465. https://doi.org/10.1016/j.jpowsour.2021.229465.